

Rotating-disk-type flow over loose boundaries

Peter J. Thomas · Farzam Zoueshtiagh

Received: 4 April 2006 / Accepted: 22 August 2006 / Published online: 10 November 2006
© Springer Science+Business Media B.V. 2006

Abstract Rotating-disk-type flow of a liquid over a loose boundary, such as a layer of sand, is investigated. For this flow the formation of a new large-scale spiral pattern has been discovered. The new pattern is reminiscent of the Type-I spiral-vortex structures which characterize the laminar–turbulent transition region of boundary layers over rigid rotating disks. Flow visualizations reveal that the new pattern and the Type-I spiral vortices co-exist in the loose-boundary flow. The research investigating the origin of the new large-scale pattern is reviewed. Then photographs from flow visualizations are analysed to obtain estimates for the critical Reynolds number for which Type-I spiral vortices first appear for the loose-boundary flow and for the critical Reynolds numbers for the laminar–turbulent transition of the boundary layer. The results suggest that Type-I vortices appear at much lower Reynolds numbers over loose boundaries in comparison with flow over rigid rotating disks and that transition also appears to be advanced to much lower Reynolds numbers. The discussion of the results suggests that advanced transition arises from disturbances introduced into the flow after the loose boundary has been mobilized and not from disturbances associated with the roughness that the surfaces of the granular layer represents to the flow while grains are at rest.

Keywords Loose-boundary flow · Ripple formation · Rotating-disk flow

1 Introduction

Loose-boundary flows are ubiquitous in nature and technology. Examples include, for instance, flow over granular beds in channels, soil erosion, flow in rivers or coastal processes [1]. Here we discuss the motion of a liquid over a granular, loose boundary in an experiment that represents a rotating-disk-type flow. The flow gives rise to the formation of ripple patterns similar to the type of sand ripples commonly observed to form on beaches, in the desert or on the bottom of the ocean. We presume that most readers of the present special theme issue on rotating-disk flow will probably not be familiar with the literature on ripple

P. J. Thomas (✉)

Fluid Dynamics Research Centre, School of Engineering, University of Warwick, Coventry CV4 7AL, UK
e-mail: pjt1@eng.warwick.ac.uk

F. Zoueshtiagh

Laboratoire de Mécanique de Lille, Bd Paul Langevin, Cité Scientifique, 59655 Villeneuve d'Ascq, France

formation. Hence, we will give a brief overview of some of the key issues associated with research on ripple formation before discussing how it relates to rotating-disk flow in the context of the experiments discussed here.

When a gas or a liquid flows over an underlying expanse of loose, granular material, one often observes the formation of characteristic, depositional bedforms known as sand ripples. Modern studies investigating these patterns, and the associated physical mechanisms leading to their formation, originate with the seminal work of Bagnold [2]. Fundamental aspects relating to the subject and the research developments in the field were summarized in [1–6].

Air-flow and liquid-flow induced ripple patterns differ from one another and they are classified as aeolian and fluvial ripples, respectively. In general, however, sand ripples typically comprise relatively small-scale features composed of fine-grained sand particles with diameters around or below one millimeter. The ripples have a wavy, often asymmetric, cross-sectional surface profile and they are usually aligned transversely to the flow direction. The typical ripple wavelength ranges between a few millimetres and several tens of centimetres with associated maximum amplitudes up to about a few centimetres [1–5]. Ripple-pattern characteristics are usually non-stationary; their cross-section profile and their wavelength have, for instance, been observed to evolve with time [7, 8].

Due to the large variety of different patterns observed, there does not, however, exist a commonly accepted, unique definition of what, in fact, constitutes a sand ripple. Lancaster [5, p. 39] points out, for instance, that Sharp [9] and Fryberger et al. [10] discuss aeolian structures composed of coarse sand or granules with median sizes in the range 1–4 mm, wavelengths as long as 0.5–2 m and amplitudes of 0.1 m or more and they refer to them as granule ripples, or as megaripples in the case of Greeley and Iversen [11]. Various other terminologies have been introduced [4, Chapter 4] in attempts to classify patterns according to their anticipated physical origins (e.g. rolling-grain ripples, vortex ripples) or their appearance (e.g. two-dimensional vortex ripples, three-dimensional vortex ripples, brick-pattern ripples, catenary ripples, lunate ripples). Nevertheless, many details of the physical mechanisms resulting in the different types of ripple patterns are not yet understood.

Well-known examples of aeolian ripples are those ripples observed in deserts while typical fluvial ripples are encountered on the bottom of the ocean or on beaches. Evidently, the formation of ripples necessitates that the granular material is set in motion by the flow above it. Consequently, the ripple-formation process is often closely associated with environmental issues such as soil erosion or sediment transport by streams and rivers as well as with industrial applications including, for instance, materials handling. The literature on the subject is vast and, as Raudkivi [1] points out, it is scattered in publications and reports in which the emphasis varies according to the area of interest. New results appear, for instance, in the contexts of sedimentology, paleontology, mineralogy, oceanography, coastal sedimentary environments, geography, agriculture, civil engineering or mining.

The present study is concerned with the early stages in the formation of fluvial ripples. Laboratory studies investigating aspects associated with such ripples often employ water channels [12–15] for this purpose. Water-channel studies can be inconvenient and laborious if large parameter ranges of the governing independent parameters, such as particle size, density and flow velocity have to be explored. Further, in water channels influences arising from the presence of the side walls of the facility can affect the flow and bias the ripple-formation process. Here we review our results obtained in a new type of system which has advantages over traditional water channels. In our new system ripples form in a granular matter underlying a rotating-disk-type flow.

Under rotating-disk flow one understands the mean flow of a wide class of boundary-layer flows established whenever there exists a differential rotation rate between a fluid and an (infinite) surface with the fluid being at rest or in a state of rigid-body rotation far above the surface [16]. Three particular cases of this family of flows are known as von Kármán, Bödewadt and Ekman flows [16, 17, Chapter 3]. When a disk rotates under a fluid which is stationary far above the disk one speaks of von Kármán flow. When a fluid rotates above a stationary disk the flow is referred to as Bödewadt flow. When disk and fluid co-rotate

with approximately equal rotation rates, the flow is classified as Ekman flow. The majority of experiments we conducted are von Kármán flows or flows of Ekman type but with differential rotation rates too large to be considered as approximately equal. There is not yet an established name for the latter category, but Lingwood [16] used the terminology BEK flow for these flows. Batchelor [18] discussed BEK flows qualitatively, while Rogers and Lance [19] and Faller [20] obtained quantitative solutions for them.

The laminar–turbulent transition region of boundary layers over rotating disks is characterized by the appearance of the characteristic, well-known 28–34 spiral vortices associated with the Type-I (Class B in some older publications) instability mode. Flow visualizations of this spiral-vortex pattern were published, for instance, in [21–26]. For the loose-boundary flow investigated here we have observed the formation of a hitherto unknown spiral pattern with an appearance not dissimilar to that of the Type-I spiral-vortex pattern but displaying 7–110 large-scale spiral arms. The new pattern is established when the granular material which forms the loose boundary is set in motion and rearranges itself driven by the fluid flow above it. The 28–34 Type-I vortex spirals are superposed onto this new pattern and can be clearly seen during the reorganization process of the granular material.

In comparison with flow over a rigid rotating disk the boundary conditions in our experiment are substantially modified. For a rigid disk the fluid has to satisfy the no-slip condition at the disk surface. This leads to an inflexion point in the velocity profile of the radial flow component. Because of Rayleigh's point-of-inflexion criterion [27, p. 432], this profile is then unstable which, in turn, results in the formation of the Type-I spiral vortices. In our experiments the granular material at the interface between the granular layer and the fluid above it is set into motion. This constitutes a potential mechanism which can remove the requirement for the no-slip condition entirely or, at least, modify it substantially. Consequently one might expect that the Type-I instability mode and its spiral-vortex pattern will be substantially affected. However, our experiments show that the qualitative nature of the Type-I instability is remarkably insensitive to the changed boundary conditions.

The relevance of our research, in the context of this special theme issue on rotating-disk flow, is that it approaches the flow from an angle that is entirely different from that of previous studies. While our own main interests to date focused on the origins of the new large-scale spiral pattern, our experiment gives rise to a rotating-disk-type flow. However, in the long run it will necessitate combining knowledge on classic rotating-disk flow with that of particle-laden flows, ripple formation in granular systems and loose-boundary hydraulics. Such new perspectives may, in the future, inspire entirely new research directions.

The details of the results summarized here that relate to our new spiral pattern are contained in our earlier publications and, wherever relevant, the reader is referred to these. The purpose of the present paper is twofold. Firstly, we introduce our work to the rotating-disk research community in order to highlight the relevance of our results in the context of classic rotating-disk flow. Secondly, we will discuss some new aspects of the flow, addressing issues which relate specifically to the laminar–turbulent transition process of the boundary layer in rotating disk-type flow over a loose boundary.

2 Experimental set-up and techniques

Our experiments were conducted in a circular fluid-filled tank (radius $R \approx 0.5$ m) positioned on a rotating turntable as illustrated in Fig. 1. Prior to the experiment small granules, such as sand, are distributed in a thin (3–30 mm deep) uniform layer on the bottom of the tank. Particles with average grain diameters $0.305 \text{ mm} \leq d_G \leq 2.65 \text{ mm}$ and densities $1.8 \text{ g cm}^{-3} \leq \rho_G \leq 7.9 \text{ g cm}^{-3}$ were used. The tank is then gradually spun up to a rotation rate ω_0 . The spin-up process is slow enough to ensure that the granules are not set in motion during this initial, preparatory phase for the experiment. Once at ω_0 , the system is allowed to settle and adopt rigid-body rotation. Now the granules on the bottom of the tank and the fluid above it do not move relative to each other and the actual experiment can begin.

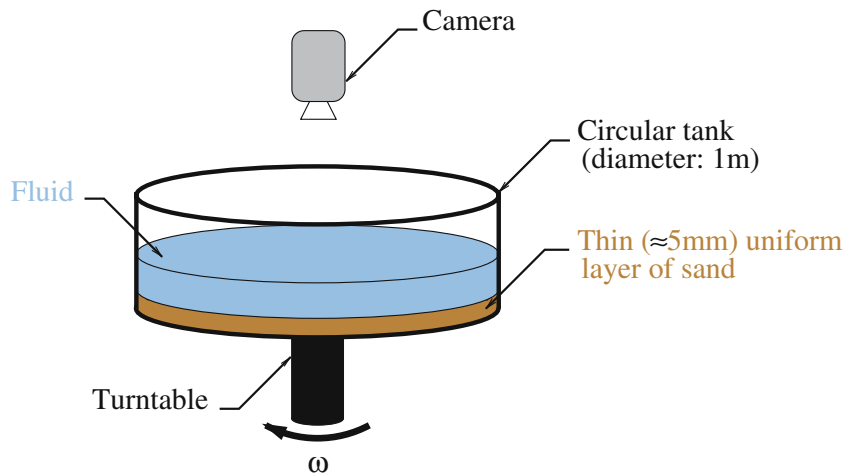


Fig. 1 Sketch of the experimental setup

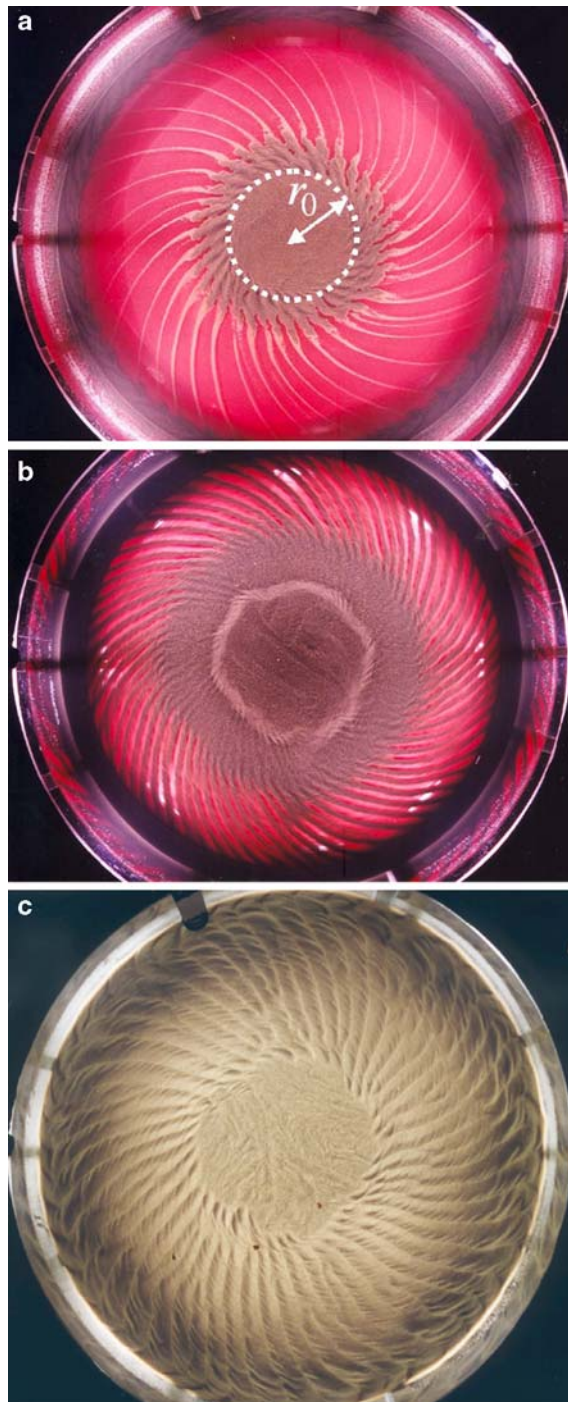
For the experiment the turntable is instantaneously spun up from ω_0 , by an increment $\Delta\omega$, to a higher rotation rate, ω_1 . Due to its inertia the fluid inside the tank cannot follow the instantaneous spin-up of the tank which has the granules resting on its bottom. A fluid boundary layer is initially established over the loose-boundary granular layer. This results in shear forces acting on the granules forming the surface of the granular layer. If the increment $\Delta\omega$ is sufficiently large, then shear forces become high enough to mobilize these granules. They begin to slide across the bottom of the tank and initiate the ripple-pattern formation process which has been the main subject of our research.

When the tank is spun up from rest, $\omega_0 = 0$, to a higher velocity ω_1 , the bottom of the tank effectively rotates underneath the stationary fluid above it and this resembles a von Kármán flow. When the tank is accelerated from a velocity $\omega_0 \neq 0$ to a higher velocity ω_1 , the resulting flow is of Ekman type where fluid and disk co-rotate. However, since the value of $\Delta\omega = \omega_1 - \omega_0$ required to mobilize the grains has to be relatively large, the flow is, in the terminology of Lingwood [16], a BEK flow and not an Ekman flow. Finally, when the tank is suddenly brought to rest from an initial rotation rate ω_0 , a Bödewadt-type flow is established. The values of ω_0 and ω_1 ranged between 0 rad s^{-1} and 5 rad s^{-1} . Hence, $\Delta\omega = \omega_1 - \omega_0$, was within $0 \text{ rad s}^{-1} < \Delta\omega < 5 \text{ rad s}^{-1}$ in spin-up and has corresponding negative values in spin-down experiments when the rotational velocity is decreased.

3 Typical spiral patterns observed in experiment for loose-boundary flow

Figure 2(a)–(c) illustrate three typical large-scale spiral patterns formed as a result of the re-organization process of the granular material on the bottom of the tank when the turntable is spun up by an increment $\Delta\omega$ that is large enough to initiate granule motion. The patterns are fully formed within 10–20 s of the spin-up of the tank. Depending on the experimental conditions, patterns with $7 \leq n \leq 110$ spiral arms originating from a uniform, circular granule patch of radius r_0 located in the centre of the tank develop. The number of spiral arms was determined by counting the arms at radii just outside the central granule patch. In some experiments we observed dislocations associated with arms that had not fully formed. The error for the number of arms associated with such dislocations is typically ± 1 for small values of n and maximum errors for largest n do not exceed approximately ± 3 . Granules located inside the central patch, $r < r_0$, appear to remain unaffected by the ongoing reorganization process on its outside. Both n and r_0 are independent of time and the data analysis has revealed that $n \propto \Delta\omega^{-1}$ and $r_0 \propto \Delta\omega^{-1}$.

Fig. 2 Spiral pattern observed in an experiment with (a) $\Delta\omega = 1.8 \text{ rad s}^{-1}$, $\omega_1 = 3.2 \text{ rad s}^{-1}$, initial height of the granule layer about 5 mm, (b) $\Delta\omega = 1.3 \text{ rad s}^{-1}$, $\omega_1 = 4.0 \text{ rad s}^{-1}$, initial height of the granule layer about 5 mm, (c) $\Delta\omega = 1.02 \text{ rad s}^{-1}$, $\omega_1 = 3.54 \text{ rad s}^{-1}$, initial height of the granule layer about 30 mm. The turntable is rotating clockwise



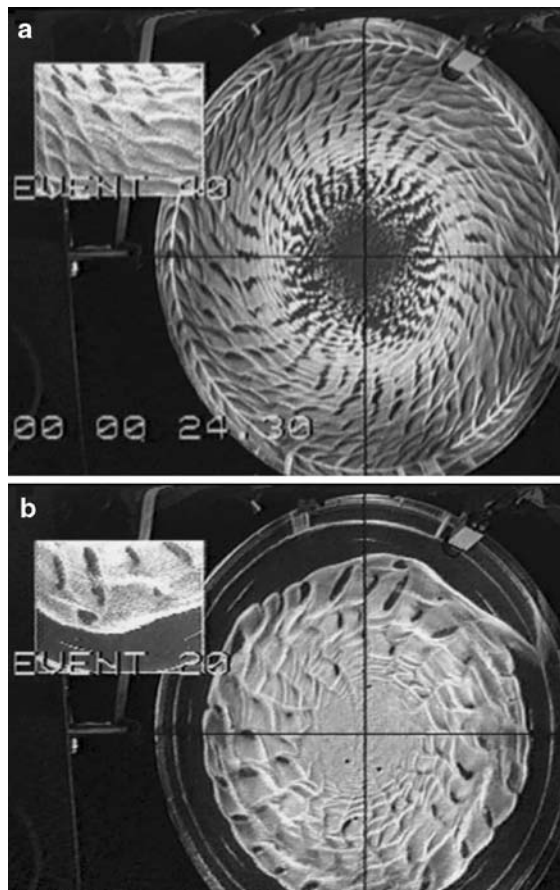
Since granules only move at locations $r > r_0$, the critical radius, r_0 , corresponds to that location where the forces acting on the grains on the surface of the granule layer are just sufficient to initiate granule motion. This implies that the developing spiral arms should initially constitute structures corresponding to those referred to as rolling-grain ripples in the literature on sedimentary structures in non-rotating systems [4, p. 125]. However, we have clearly observed recirculating motion of grains behind

ripples a few seconds after the pattern formation process is first initiated. This would indicate that the spiral arms represent vortex ripples. We believe that the observed spiral arms are initially formed as rolling-grain ripples and subsequently develop into vortex ripples once the height of the crests becomes sufficiently large. However, we do not have any further experimental evidence available to support this speculation.

The patterns in Fig. 2(a) and (b) were formed from a granule layer with an initial granule-layer thickness of about 5 mm while Fig. 2(c) displays a pattern in a deeper layer with an initial thickness of about 30 mm. Further other photos of similar spiral patterns are contained in [28, 29] and in [30, p. 35]. In Fig. 2(a) and (b) the initial granule layer was not deep enough to ensure that the bottom of the tank remained completely covered during the pattern-formation process. For $r > r_0$, large areas between successive spiral arms are entirely granule-free. This is not the case when the initial layer is deep enough as for the experiment in Fig. 2(c).

In all our previous publications we only considered spiral-arm formation in spin-up experiments, i.e., in experiments where the rotation rate of the turntable was increased from a value ω_0 to a higher value ω_1 . However, we have also performed a number of spin-down experiments for which $\omega_0 > \omega_1$. For spin-down experiments ripple patterns are also formed but their structures are usually less regular and their appearance is more complex than the relatively simple spiral patterns of Fig. 2. This is illustrated in Fig. 3 which displays two typical patterns generated in spin-down experiments.

Fig. 3 Spiral pattern observed in spin-down experiments for deceleration from (a) $\omega_0 = 2.55 \text{ rad s}^{-1}$ to $\omega_1 = 1.58 \text{ rad s}^{-1}$ with $\Delta\omega = -0.97 \text{ rad s}^{-1}$, (b) $\omega_0 = 3.11 \text{ rad s}^{-1}$ to $\omega_1 = 1.57 \text{ rad s}^{-1}$ with $\Delta\omega = -1.54 \text{ rad s}^{-1}$. Fluid and turntable are both rotating clockwise but fluid rotates faster than the tank



4 Modelling the large-scale spiral pattern and comparison to experimental data

4.1 Computational model

Thomas and Zoueshtiagh [29, 31] developed a cellular-automaton model to simulate the observed spiral-ripple patterns computationally. The simulation is based on the adaptation of a model originally introduced by Nishimori and Ouchi [32] to model ripple formation in a straight channel. The model constitutes an algorithm by which grains are moved around a computational domain according to simple rules. The rules simulate saltation [2, p. 19], [4, Chapter 6.9.1] and creep [32] which are assumed to be the two mechanisms responsible for grain transport. The rules also incorporate control parameters representing aspects such as the shear stress imposed on the sand surface by the fluid moving above it or the mean flow velocity experienced by a grain during its saltation flight. For instance, the flight length will be the longer the higher its starting point in the computational domain.

The model does not incorporate effects resulting from quantities such as the grain size, grain density or the grain shape and its surface properties. These are evidently important as regards the absolute ripple wavelength. However, our goal was not to provide a realistic model for this absolute wavelength. The goal was to explain the experimentally measured scalings, $n \propto \Delta\omega^{-1}$ and $r_0 \propto \Delta\omega^{-1}$ and these are found to be independent of the physical characteristics of the grains. Similarly, Coriolis forces can be incorporated but the data analysis of Zoueshtiagh and Thomas [31] has shown that they are not required to explain the measured scalings.

4.2 Computational patterns

Figure 4(a) and (b) display two computationally generated patterns for $\Delta\omega = 5$ and $\Delta\omega = 11$, respectively. Here $\Delta\omega$ is specified in arbitrary, non-dimensional units and not in units of rad s^{-1} as is the case in the experiments. The patterns do not display a spiral structure because the Coriolis term was inactive in both cases. The colour scale in the figures (online only) characterizes the stacking height of the granules at a particular lattice site in the computational domain. Red identifies ripple crests while blue represents troughs (grey scale in print).

Figure 4(a) and (b) show a decreasing number n of arms for increasing $\Delta\omega$. The arms originate from an inner patch whose radius decreases with increasing $\Delta\omega$. These results are qualitatively consistent with the experimental observations.

4.3 Comparison of computational and experimental results

Figure 5 compares measured and computed results for the number, n , of spiral arms as a function of the velocity increment, $\Delta\omega$. The main result expressed by Fig. 5 is that the experimentally observed scaling, $n \propto \Delta\omega^{-1.0}$, is reproduced by the model.

In Fig. 5 experiment and computation differ by an arbitrary constant, reflecting the fact that the computational model does not account for physical properties such as, for instance, the grain size or the grain density. The figure displays three alternative power-law-type interpolations of the computational data points. The purpose of three alternative fits is to provide some means for evaluating the error associated with the exponent of the $\Delta\omega$ -scaling; for further details see [31]. This paper also contains a graph revealing a similarly good agreement between experiment and computation for the scaling of the radius, r_0 , of the inner patch with $\Delta\omega$.

Our model with its simple rules to move grains is, evidently, far too naive to realistically simulate the complicated interactive fluid-granule dynamics. Consequently, the agreement of experiment and computation unlikely arose as a consequence of the particular rules specified for the grain motion. This observation

Fig. 4 Two computational ripple patterns. The flow speed $v(r)$ at radius r is $v(r) = \Delta\omega r$ where $\Delta\omega$ is specified in arbitrary units. For the two figures shown the values of $\Delta\omega$ were
(a) $\Delta\omega = 5$ and
(b) $\Delta\omega = 11$

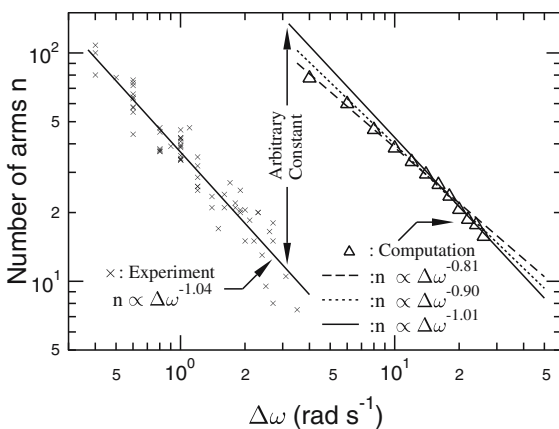
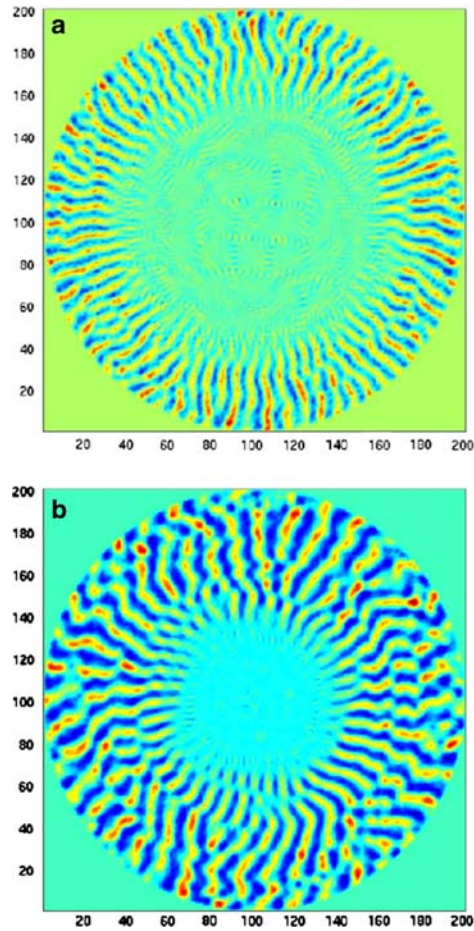


Fig. 5 Comparison of experiment and computation. The number, n , of ripples developing as a function of the velocity increment, $\Delta\omega$

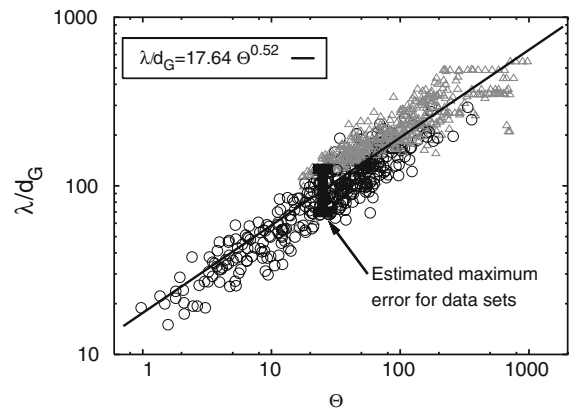


Fig. 6 Non-dimensional ripple wavelength λ/d_G as a function of the mobility parameter Θ . Comparison of data from present experiments in rotating system with data of other authors for ripple formation in non-rotating systems. Full references for the data used for comparison are included in main body of text

led Zoueshtiagh and Thomas [31, 33] to one of their key conclusions. The scalings arise necessarily as a consequence of the circular geometry in conjunction with the existence of critical onset thresholds for pattern formation in experiment and model. Hence, the rules used to move the grains and, in fact, their motion itself are irrelevant to the wavelength scaling at the onset location, i.e., at the edge r_0 of the inner patch.

4.4 Comparison of data for rotating and non-rotating systems

The experimental data obtained by Zoueshtiagh [29] for the rotating system described in Sect. 2 are compared to comprehensive data sets for ripple formation in a number of different non-rotating systems in unidirectional [34, 35] as well as oscillatory [15, 36, 37] flow. All data are from experiments where the ripples are observed to form within a few seconds. Thus, the data comparison is restricted to transitional ripples during the early stage of their evolution.

Data comparison is facilitated by non-dimensionalizing the ripple wavelength, λ , using the grain diameter, d_G , and displaying this ratio λ/d_G as a function of a mobility parameter Θ defined as

$$\Theta = \frac{\rho_G U^2}{g(\rho_G - \rho_F) d_G} = \frac{U^2}{g' d_G}. \tag{1}$$

In Eq. 1 the quantity U is a typical velocity scale characterizing the flow velocity above the granule layer, ρ_F is the fluid density and $g' = g(\rho_G - \rho_F)/\rho_G$ is the reduced gravity. For our present system this velocity is $U = \Delta\omega r_0$. For details concerning the values of U for the data used for comparison see [38].

Figure 6 displays approximately four hundred data points (circles) from our own experiments in the rotating system in comparison to around five hundred data points (triangles) from non-rotating experiments. The data in Fig. 6 cover approximate parameter ranges for particle size and density of $0.11 \text{ mm} \leq d_G \leq 3.17 \text{ mm}$ and $1.28 \text{ g cm}^{-3} \leq \rho_G \leq 7.9 \text{ g cm}^{-3}$. The figure reveals that the data points of all systems collapse on one line. The line interpolating the data in Fig. 6 represents a least-squares fit to all nine hundred data points and is given by $\lambda/d_G = 17.64 \times \Theta^{0.52}$. From this one concludes $n \propto \Delta\omega^{-1.04}$, which re-confirms the scaling already revealed by Fig. 5. In summary, Fig. 6 shows that the ripple patterns in our rotating system obey the same scaling one observes for sand ripples in non-rotating systems implying that they constitute a rotating analogue of such sand-ripples [38].

5 Type-I spiral vortices in loose-boundary flow

Figure 7 shows a photograph taken a few seconds after the speed of the turntable was increased. At this instant the difference between the velocity of the bottom of the tank and the fluid above it is large and the granular material is re-organizing itself to form the type of large-scale granular spiral arms seen in Fig. 2(a)–(c). Figure 7 clearly reveals the presence of the characteristic Type-I spiral-vortex pattern. The photo shows that the Type-I vortices co-exists with the forming large-scale granular spiral arms and that both intersect each other at angles roughly of the order of $50^\circ - 90^\circ$. The photo also shows that the Type-I vortices first appear in the immediate vicinity of the boundary of the central granule patch from which the large scale spiral arms originate.

While Fig. 7 shows a flow shortly after the spin-up of the tank, Fig. 8 displays a corresponding photograph for a spin-down experiment (Bödewadt flow). In this case the type of large-scale granular spiral patterns of Fig. 2(a)–(c) and Fig. 7 are not formed. However, Fig. 8 clearly documents the existence of Type-I spiral vortices while the granules are in the process of being transported to the centre of the tank.

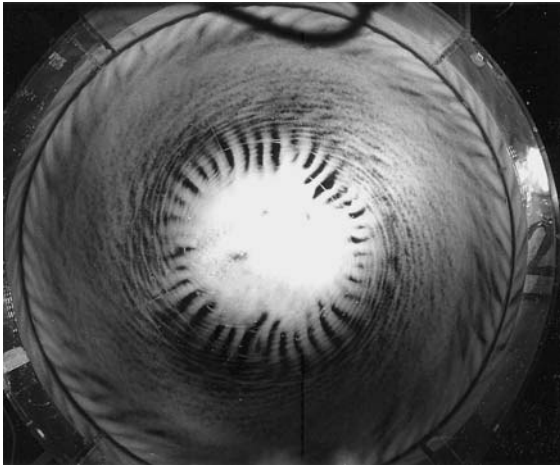


Fig. 7 Photo showing Type-I vortices co-existing with granular spirals during the formation process of the large-scale spiral arms in a spin-up experiment with $\omega_0 = 2.6 \text{ rad s}^{-1}$ and $\omega_1 = 3.5 \text{ rad s}^{-1}$. Turntable rotating anti-clockwise

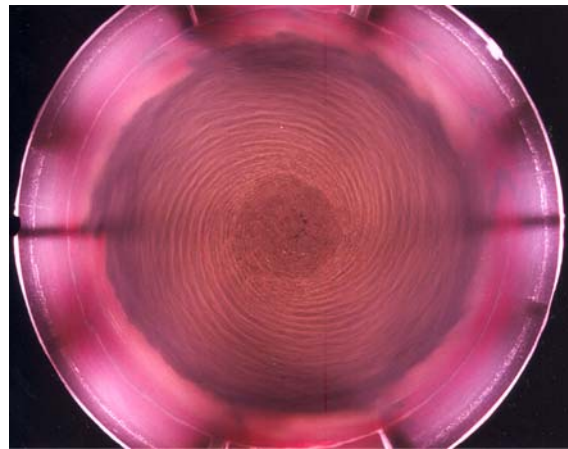


Fig. 8 Type-I vortices in a spin-down experiment from $\omega_0 = 4.05 \text{ rad s}^{-1}$ to $\omega_1 = 0 \text{ rad s}^{-1}$. In spin-down experiments the type of large-scale granular spiral arms seen in Fig. 2(a)–(c) and Fig. 7 are not formed. Turntable at rest, fluid rotating clockwise

Figure 2(a)–(c) displayed the large-scale granular spiral-ripple pattern several seconds after the end of its formation process. At this stage one can often see faint striations imprinted into the surface of the granular layer as shown in Fig. 9. The origin of the striations is not entirely clear. While they may be due to the Type-I vortices they may, alternatively, be caused by Görtler vortices [27, pp. 481–482] generated when the fluid flows through the troughs connecting successive large-scale granular spiral arms.

6 Spiralling angle of Type-I vortices and large-scale spiral arms

We have developed a Matlab computer program [29] which can determine the spiralling angle, $\epsilon(r)$, of Type-I vortices and of our large-scale granular spiral arms from scanned, electronic versions of photographs. The spiralling angle is the angle with respect to the azimuthal direction. We tested the program by analysing the well-known photograph showing Type-I spiral vortices over a rotating disk displayed as Fig. 7 in [24] and reproduced as [25, Fig. 30]. A very similar photo is also shown in [26, 39, 40]. In order to include some typical values for the spiralling angle for large-scale granular spiral arms, we analysed the photograph shown as [28, Fig. 2(b)] with our program.

In the literature the values for the spiralling angle for the Type-I vortices are usually quoted as having typical values in the range $11^\circ \leq \epsilon \leq 20^\circ$ [26]. Kobayashi et al. [24] state that they found somewhat scattering values for ϵ but they clearly observed that the value of the angle decreases from $15^\circ \sim 13^\circ$ to about 7° as the local Reynolds number increases. Kobayashi et al. [24] define the Reynolds number for their von Kármán flow as

$$\text{Re} = r^2 \omega / \nu, \quad (2)$$

where r is the distance from the axis of rotation, ω is the rotational velocity of the disk and ν is the kinematic viscosity. For the data of Kobayashi et al. [24] the disk in their Fig. 7 was rotating at 1,800 rpm yielding $\omega = 188.5 \text{ rad s}^{-1}$. They do not provide a value for ν , but from the data in the table of their Fig. 9 it can be inferred that they used $\nu = 15 \text{ mm}^2 \text{ s}^{-1}$. This is the standard value for the kinematic viscosity of air at 20°C and this value was used to calculate the Reynolds numbers for Fig. 10.

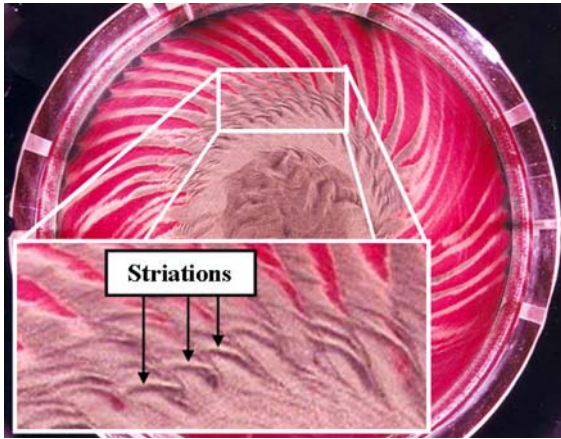


Fig. 9 Photo showing striations imprinted into the surface of the granular layer, $\omega_0 = 1.78 \text{ rad s}^{-1}$ and $\omega_1 = 2.82 \text{ rad s}^{-1}$

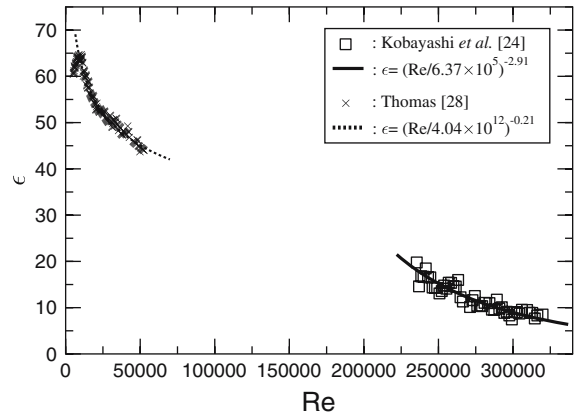


Fig. 10 Spiralling angle, ϵ , as function of Reynolds number, Re . Data obtained with Matlab program by analysing electronic versions of Fig. 7 of Kobayashi et al. [24] showing Type-I vortices and Fig. 2(b) of Thomas [28] showing large-scale granular spiral arms.

Figure 10 displays data for the spiralling angle, ϵ , as obtained with our computer program. The figure reveals that the value of ϵ , for the Type-I vortices of Kobayashi et al. [24] decreases from 20° to about 7° in the range between, approximately, $Re = 2.3 \times 10^5$ and $Re = 3.5 \times 10^5$. However, due to the data scatter, the original six data points shown in Fig. 11 of Kobayashi et al. [24] do not reveal the exact nature of the decrease of ϵ with Re . The data obtained with our Matlab program illustrate this much clearer. The interpolation identified in Fig. 10 by the solid line represents a linear fit of type $y = mx + b$ in coordinates $y = (\epsilon)$ and $x = (Re)$. The fitting routine yielded values of $m = -2.91$ and $b = 38.9$ and with these the data fit can be re-written as $\epsilon = (Re/6.37 \times 10^5)^{-2.91}$. This expression is not intended to imply the existence of power-law scaling for $\epsilon(Re)$. The range of the available data is, of course, much too narrow to infer any power-law scaling; the expression only represents a least-squares summary of the data points.

For the photograph shown as Fig. 2(b) in [28] the spin-up initiating large-scale spiral-arm formation was from $\omega_0 = 1.8 \text{ rad s}^{-1}$ to $\omega_1 = 3.4 \text{ rad s}^{-1}$. Since this represents a BEK flow, we use a Reynolds number

$$Re = \frac{r^2 \Delta\Omega_*^2 l^2}{\nu^2} \tag{3}$$

based on the definition introduced by Faller [20]. In Eq. 3 $\Delta\Omega_* = \Omega_F - \Omega_D$, and $l = (\nu/\Omega)^{1/2}$. The velocity Ω is

$$\Omega = \frac{\Omega_F + \Omega_D}{4} + \left(\left(\frac{\Omega_F + \Omega_D}{4} \right)^2 + \frac{(\Delta\Omega_*)^2}{2} \right)^{1/2} \tag{4}$$

and represents a system rotation rate. Note that Eq. 3 becomes Eq. 2 when $\Omega_F = 0$ or when $\Omega_D = 0$. For Fig. 2(b) in [28] one has $\Omega_F \equiv \omega_0$ and $\Omega_D \equiv \omega_1$. The fluid in the experiments of Thomas [28] was saturated salt water for which the data tabulated in Lide [41, pp. 8–71] give $\nu = 1.7 \text{ mm}^2 \text{ s}^{-1}$.

Figure 10 displays $\epsilon(r)$, for the large-scale granular spiral arms shown in [28, Fig. 2(b)], in the top left corner of the graph. These data represent some typical values for the spiralling angle. The angle ϵ depends on ω_0 and ω_1 and can, in fact, be seen to develop continuously during the formation phase of the spiral arms. However, the data show that ϵ is substantially larger for the large-scale spiral arms than for Type-I vortices. Figure 10 shows that ϵ decreases for the spiral arms and for Type-I vortices in a similar way.

Spalart [42] states that the Type-I spirals follow logarithmic spirals. We found that the shape of the large-scale spiral arms can also be approximated by logarithmic spirals which have their centres located near the boundary of the central granule patch. The data fit interpolating the spiral-arm data (dotted line) in Fig. 10 represents a least-squares fit obtained analogous to that for the Type-I vortices and can be written as $\epsilon = (\text{Re}/4.04 \times 10^{12})^{-0.21}$. Note that the first few data points for $\text{Re} \leq 10500$, where ϵ initially increases from about 60° to 65° , are not included in the data fit.

We do not yet have a definitive explanation why ϵ in Fig. 10 initially increases for the data of Thomas [28]. However, the magnitude of the radial interval, Δr , over which the increase of ϵ takes place may represent the length scale on which system rotation becomes important to the grain dynamics. This can be seen as follows. The time, t_ω , for one revolution of a system rotating with rotational velocity ω is equal to $t_\omega = 2\pi/\omega$. The time, t_r , taken by a particle to cover a radial distance ΔR at speed u_r is $t_r = \Delta R/u_r$. Rotation will be important when [43, Chapter 1–5] $t_\omega/t_r = 2\pi u_r/\omega \Delta R \lesssim 1$. From this one concludes that the lengthscale for which rotation becomes important is $\Delta R \gtrsim 2\pi u_r/\omega$. A typical value for the magnitude of the depth-averaged radial velocity, u_r , in laminar or in turbulent rotating-disk boundary layers, is estimated from the data plotted in [17, Fig. 3.4]; it is roughly of the order of $u_r = 0.06\omega r$. Hence, one requires $\Delta R \gtrsim 2\pi 0.06r$ for rotation to become important to the grain dynamics. Since the radius of the inner granule patch in [28, Fig. 2(b)] is approximately 100 mm one finds $\Delta R \gtrsim 2\pi 0.06 100 \text{ mm} \approx 38 \text{ mm}$. The data in Fig. 10, for which the angle ϵ for the spirals of Thomas [28] initially increases, correspond to a radial interval of $\Delta r \approx 45 \text{ mm}$. Hence, Δr and ΔR are of the same order of magnitude, but Coriolis effects are only important when Δr exceeds the scale ΔR .

7 Critical Reynolds numbers for appearance of Type-I vortices and transition for loose-boundary flow

The first appearance of Type-I vortices in rotating-disk flow indicates the beginning of the laminar–turbulent transition process of the boundary-layer flow. Our data in Fig. 10, for the Type-I vortices of Kobayashi et al. [24], show that the associated critical Reynolds number for the first appearance of the vortices is of the order of $\text{Re} = 2.3 \times 10^5$. This value is consistent with the minimum critical value $\text{Re} = 8.24 \times 10^4$ found by Wilkinson and Malik [44] from hot-wire measurements and predicted theoretically by Mack [45]. However, Fig. 10 also shows that large-scale spiral arms exist at substantially lower Reynolds numbers. If transition over the loose boundary would occur at the same Reynolds numbers as in flow over rigid smooth disks, then Fig. 10 would imply that the large-scale spiral arms form in the laminar flow regime. However, Fig. 7 reveals this is not the case!

In Fig. 7 one can clearly identify Type-I vortices just outside the central granule patch. The radius of the tank in Fig. 7 is 0.5 m and, hence, one infers that Type-I vortices are present at $r \geq 0.15 \text{ m}$. For Fig. 7 one has $\omega_0 = 2.6 \text{ rad s}^{-1}$ and $\omega_1 = 3.5 \text{ rad s}^{-1}$ such that $\Delta\omega \equiv -\Delta\Omega_* = 0.9 \text{ rad s}^{-1}$ which yields $\Omega = 3.18$ and a critical Reynolds number $\text{Re} = 3371$. Similarly one can infer that for the spin-down flow in Fig. 8 that Type-I vortices exist for $r \geq 0.08 \text{ m}$. In the experiments the tank was decelerated to come to rest from an initial rotation rate of $\omega_0 = 4.05 \text{ rad s}^{-1}$ and, hence, one finds an associated critical Reynolds number $\text{Re} = 15247$. Since these two critical Reynolds-number values for the first appearance of Type-I vortices in loose-boundary flow are based on estimates obtained from flow visualizations, they probably overestimate the true critical Reynolds number. In any case, one can conclude that the critical Reynolds number for appearance of Type-I vortices for the flow over loose boundaries is at least one order of magnitude smaller than the corresponding value of $\text{Re} = 8.24 \times 10^4$ found by Wilkinson and Malik [44] and Mack [45] for flow over smooth, rigid disks.

Since the critical Reynolds number for the appearance of Type-I vortices is substantially reduced for the flow over the loose boundary, one expects that the associated transitional Reynolds number will be reduced correspondingly. For flow over rigid rotating disks the boundary has become fully turbulent at

radial positions where Type-I vortices can no longer be observed. It is plausible to assume that this is also the case for loose-boundary flow. In Fig. 7 one cannot see Type-I vortices for locations $r \geq 0.34$ m corresponding to $Re = 1.73 \times 10^4$. Similarly, in Fig. 8 Type-I vortices are not visible above $r \geq 0.28$ m which here corresponds to $Re = 1.9 \times 10^5$. Both these values for the critical Reynolds number for laminar–turbulent transition in loose-boundary flow are substantially lower than the corresponding value of $Re = 2.632 \times 10^5$ stated by Lingwood [46] for rigid-disk flow.

8 Reason for the reduced critical Reynolds numbers for loose-boundary flow

There are two obvious potential reasons for the earlier appearance of Type-I vortices in loose-boundary flow and the associated lower transitional Reynolds numbers. Growth of Type-I vortices and transition might be promoted by the roughness which the surface of the granular layer, within the central granule patch from which the spiral arms originate, represents to the flow above it. Within the central patch the granules do not move and disturbances may be caused by roughness alone when the fluid flows over the surface of the granular bed. Alternatively, advanced transition may be due to the generation of disturbances created after the particles have been mobilized and when they are, possibly, partially entrained into the boundary layer and collide and interact with other particles.

Zoueshtiagh et al. [47] investigated the flow over rough rotating disks. They carried out observations to determine the critical Reynolds number for the laminar–turbulent transition of the boundary layer over rough rotating disks. To this end disks were coated with uniform layers of approximately mono-disperse granular materials. Three different materials with average diameters of around $170 \mu\text{m}$, $335 \mu\text{m}$ and 1.325mm were used and experiments were carried out for rotational velocities in the range $4 \text{rad s}^{-1} \leq \omega \leq 18.85 \text{rad s}^{-1}$. The observations revealed that the transitional Reynolds number at the highest roughness level, and for all tested disk speeds, was substantially lower than the value $Re = 2.632 \times 10^5$ given by Lingwood [46] for smooth disks. Zoueshtiagh et al. [47] found that for the roughest disk at the lowest tested disk speed of 4rad s^{-1} transition occurred at $Re \approx 1.156 \times 10^5$ and this value dropped to $Re \approx 2.403 \times 10^4$ at the highest disk speed of 18.75rad s^{-1} . However, for the lower roughness levels, i.e., for disks covered with the $170 \mu\text{m}$ and $335 \mu\text{m}$ materials, the transitional Reynolds number was not significantly affected as long as the disk speed remained below 12.5rad s^{-1} . For the flows shown in Figs. 7 and 8 the approximate grain sizes were in the range $200\text{--}400 \mu\text{m}$. The rotational velocities were $\Delta\omega = 0.9 \text{rad s}^{-1}$ for the spin-up experiment of Fig. 7 and $\Delta\omega = -4.05 \text{rad s}^{-1}$ for the spin-down experiment of Fig. 8. For these values the results of Zoueshtiagh et al. [47] imply that the surface roughness of the granular layer on the bottom of the tank does not affect the transitional Reynolds number. This suggests that the appearance of Type-I vortices and the advanced transition of the loose-boundary flow is initiated by destabilizing disturbances introduced into the boundary-layer flow after the particles have been set in motion and when they collide and interact with each other.

While it was seen that Type-I vortices in flow over loose boundaries appear at substantially lower critical Reynolds numbers than for flow over rigid, smooth surfaces their number, however, is not affected by the change in the boundary conditions. We have magnified several of the type of photographs shown in Figs. 7 and 8 and we have counted the number of vortices. In each case we determined that there are between, approximately, 28 and 34 Type-I vortices present; this is the same number as that for flow over smooth, rigid disks (see for instance [24, 26]).

9 Conclusion

Experiments with rotating flow over the loose boundary formed by a layer of granular material were discussed. The experiments have shown that von Kármán-type and Ekman-type flows lead to the formation of a hitherto unknown large-scale spiral-arm pattern which forms when the granular material is set in

motion and when it reorganizes itself driven by the fluid flow above the granule layer. The newly observed pattern was found to display between 7 and 110 spiral arms and is reminiscent of the spiral pattern associated with the 28–34 characteristic Type-I spiral vortices known to exist in the laminar–turbulent transition region of the boundary layer over rigid rotating disks. We briefly reviewed our cellular automaton model [31] which reproduces the scalings measured for the characteristic geometric pattern features of the newly observed large-scale pattern. The summary of the comparison of our experimental data for this pattern with data available in the literature for sand ripples in non-rotating systems suggested that the new pattern represents a rotating equivalent of such granular ripples [38].

We have presented new flow visualizations which show that the large-scale spiral-arm pattern and the Type-I spiral vortices coexists over loose boundaries for von Kármán flow, and for Ekman-type flow in Lingwood's [16] BEK flow regime. For Bödewadt flow over a loose boundary the Type-I vortices also exist but the large-scale spiral arms are not formed. Here the developing ripple patterns are less regular and also display a more complex structure. After the large-scale spiral arms are fully formed for the von Kármán-type and Ekman-type flow one can often observe faint striations in the surface of the granular material. These striations may represent remaining evidence of the Type-I vortices, alternatively they may originate from Görtler vortices generated when fluid flows through the troughs between two neighbouring large-scale spiral arms.

The analysis of flow-visualization photographs has revealed that for loose-boundary flow the Type-I vortices first appear at Reynolds numbers substantially below those for flow over rigid, smooth rotating disks. For rigid disks they appear at radial positions corresponding to Reynolds numbers of the order of 10^5 , while we observed them over a loose boundary for Ekman-type flow at $Re = 3371$ and for Bödewadt flow at $Re = 15247$. Associated with this earlier appearance of the Type-I vortices is a reduced transitional Reynolds number. A typical value for the transitional Reynolds number for rigid, smooth disks is $Re = 2.632 \times 10^5$ [46], while our flow visualizations indicate that the loose-boundary Ekman-type flow becomes turbulent around $Re = 1.73 \times 10^4$ and for Bödewadt-type flow at $Re = 1.9 \times 10^5$. These results were compared to the measurements of Zoueshtiagh et al. [47] for transitional Reynolds numbers for flow over rough rotating disks. The comparison suggests that earlier transition of the loose-boundary flow is not caused by disturbances arising from the surface roughness of the granular layer but that it is caused by disturbances introduced into the flow after the granular material has been set in motion and when granules collide and interact with each other.

One of the referees for this paper remarked that the measured reduced Reynolds numbers for the appearance of Type-I vortices and for laminar–turbulent transition may not necessarily reflect a real destabilizing effect introduced by the loose boundary in comparison to rigid-disk flow. The referee suggested that an apparent reduction of the Reynolds numbers could potentially arise as a consequence of transient, sub-critically excited, and subsequently damped, eigenmodes in response to the increase of the rotation rate of the turntable. The suggested scenario being similar to the shedding of von Kármán-type vortices behind a circular cylinder in response to an instantaneous increase of the free-stream flow velocity at Reynolds numbers below the shedding threshold for von Kármán vortices [48]. However, it is presently entirely unclear if, or in how far, the cylinder-flow analogy suggested by the referee can hold in the present context. Nevertheless, if the Type-I eigenmode had been excited subcritically, one would expect that, immediately after the spin-up of our turntable, Type-I vortices should be visible at some radius r_1 smaller than the associated value r_R typically found for transition over rigid disks. One would then expect to observe that r_1 grows from this initial value until it finally reaches the value characteristic for rigid-disk flow. None of our flow visualizations have revealed any evidence that this is the case. However, it is possible that the type of flow visualizations analysed here are not adequate to resolve this feature if it did exist. Consequently, all we can suggest at this point is to carry out more sophisticated experiments in the future to further investigate the issue raised by the referee.

Finally, the flow visualizations for our loose-boundary flow have revealed that the overall, qualitative nature of the spiral pattern associated with the Type-I vortices is not substantially affected by the changed

boundary conditions. Similarly to flow over rigid disks one always observes between 28 and 34 Type-I spiral vortices despite the substantial reduction of the Reynolds numbers associated with their first appearance and for the transitional Reynolds number.

References

1. Raudkivi AJ (1990) Loose boundary hydraulics, 3rd edn. Pergamon Press
2. Bagnold RA (1941) The physics of blown sand and desert dunes. Methuen, London
3. Allen JRL (1984) Sedimentary structures. Elsevier, Amsterdam
4. Sleath JFA (1984) Sea bed mechanics. Wiley, New York
5. Lancaster N (1995) Geomorphology of desert dunes. Routledge, London
6. Blondeaux P (2001) Mechanics of coastal forms. *Annu Rev Fluid Mech* 33:339–370
7. Raudkivi AJ (1997) Ripples on stream bed. *J Hydraul Eng* 123:58–64
8. Stegner A, Wesfreid JE (1999) Dynamical evolution of sand ripples under water. *Phys Rev E*, 60:R3487–R3490
9. Sharp RP (1963) Wind ripples. *J Geol* 71:617–636
10. Fryberger SG, Hesp P, Hastings K (1992) Aeolian granule ripple deposits, Namibia. *Sedimentology* 39:319–331
11. Greeley R, Iversen JD (1985) Wind as a geological process. Cambridge University Press, Cambridge
12. Kennedy JF, Falcon M (1965) Wave generated sediment ripples. Hydrodynamics Laboratory Report no. 86, Department of Civil Engineering, Massachusetts Institute of Technology, MA, USA
13. Yalin MS (1965) Similarity in sediment transport by currents. Hydraulics research paper, vol. 6, Ministry of Technology, London
14. Harms J (1969) Hydraulic significance of some sand ripples. *Prog Geol Soc Am Bull* 80:363–395
15. Sleath JFA (1976) On the rolling grain ripples. *J Hydrol Res* 14:69–81
16. Lingwood RJ (1997) Absolute instability of the Ekman layer and related rotating flows. *J Fluid Mech* 331:405–428
17. Owen JM, Rogers RH (1989) Flow and heat transfer in rotating-disc systems, Volume 1 – Rotor-stator flow. Research Studies Press Ltd., John Wiley & Sons Inc.
18. Batchelor GK (1951) Note on the class of solutions of the Navier-Stokes equations representing steady non-rotationally symmetric flow. *Q J Mech Appl Math* 4:29–41
19. Rogers MH, Lance GN (1960) The rotationally symmetric flow of a viscous fluid in the presence of an infinite rotating disk. *J Fluid Mech* 7:617–631
20. Faller AJ (1991) Instability and transition of the disturbed flow over a rotating disk. *J Fluid Mech* 230:245–269
21. Gregory N, Stuart JT, Walker WS (1955) On the stability of three-dimensional boundary layers with application to the flow due to a rotating disk. *Phil Trans R Soc A* 248:155–199
22. Faller AJ (1963) An experimental study of the instability of the laminar Ekman boundary layer. *J Fluid Mech* 15:560–576
23. Tatro PR, Mollo-Christensen EL (1967) Experiments on Ekman layer instability. *J Fluid Mech* 28:531–543
24. Kobayashi R, Kohama Y, Takamadate CH (1980) Spiral vortices in boundary-layer transition regime on a rotating disk. *Acta Mech* 35:71–82
25. Wimmer M (1988) Viscous flow instabilities near rotating bodies. *Prog. Aerospace Sci* 25:43–103
26. Reed HL, Saric WS (1989) Stability of three-dimensional boundary layers. *Ann Rev Fluid Mech* 21:235–284
27. Schlichting H, Gersten K (2000) Boundary-layer theory, 8th edn. Springer
28. Thomas PJ (1994) Pattern formation of granules on the bottom of a differentially rotating tank. *J Fluid Mech* 274:23–41
29. Zoueshtiagh F (2001) Experimental and computational study of spiral patterns in granular media underneath a rotating fluid. Ph.D thesis University of Warwick, Coventry, UK
30. Zoueshtiagh F, Thomas PJ (2003) Spiral patterns formed by granular media underneath a rotating fluid. Experiment vs. computation. In: Samimy M, Breuer KS, Leal LG, Steen PH (eds) A gallery of Fluid motion Camb Univ Press
31. Zoueshtiagh F, Thomas PJ (2000) Wavelength scaling of spiral patterns formed by granular media underneath a rotating fluid. *Phys Rev E* 61:5588–5592
32. Nishimori N, Ouchi N (1993) Formation of ripple patterns and dunes by wind-blown sand. *Phys Rev Lett* 71:197–200
33. Thomas PJ, Zoueshtiagh F (2005) Granular ripples under rotating flow: a new experimental technique for studying ripples in non-rotating, geophysical applications? *Phil Trans R Soc A* 363:1663–1676
34. Coleman SE, Melville BW (1996) Initiation of bed forms on a flat sand bed. *J Hydraul Eng* 122:301–310
35. Betat A, Frette V, Rehberg I (1999) Sand ripples induced by water shear flow in an annular channel. *Phys Rev Lett* 83:88–91
36. Manohar M (1955) Mechanics of bottom sediment movement due to wave action. US Army, Beach Erosion Board, Tech. Memo
37. Scherer M, Melo F, Marder M (1999) Sand ripples in an oscillating annular sand-water cell. *Phys Fluids* 11:58–67
38. Zoueshtiagh F, Thomas PJ (2003) Universal scaling for ripple formation in granular media. *Phys Rev E* 67: 031301-1–031301-5

39. Kobayashi R (1994) Review: Laminar-to-turbulent transition of three-dimensional boundary-layers on rotating bodies. *Trans ASME. J Fluids Eng* 116:200–211
40. Kohama Y (1984) Study on boundary-layer transition on a rotating disk. *Acta Mech* 50:193–199
41. Lide DR (Editor-in-Chief) (2005) *CRC handbook of chemistry and physics*. Taylor & Francis, Boca Raton
42. Spalart PR (1991) On the cross-flow instability near a rotating disk. *Proc R Aero Soc* 22.1–22.13
43. Cushman-Roisin B (1994) *Introduction to geophysical fluid dynamics*. Prentice Hall, New Jersey, USA
44. Wilkinson SP, Malik MR (1983) Stability experiments in rotating-disk flow. *AIAA Paper* 83-1760
45. Mack LM (1985) The wave pattern produced by a point source on a rotating disk. *AIAA Paper* 85-0490
46. Lingwood RJ (1996) An experimental study of absolute instability of the rotating-disk boundary-layer flow. *J Fluid Mech* 314:373–405
47. Zoueshtiagh F, Ali R, Colley AJ, Thomas PJ, Carpenter PW (2003) Laminar-turbulent boundary-layer transition over a rough rotating disk. *Phys Fluids* 15:2441–2444
48. Le Gal P, Croquette V (2000) Visualization of the space-time impulse response of the subcritical waake of the cylinder. *Phys Rev E* 62:4424–4426